https://doi.org/10.1016/j.apsusc.2023.156478

Nanoscale insights into the interfacial characteristics between calcium silicate hydrate and silica

Ming-Feng Kai[1], Florence Sanchez[2], Dong-Shuai Hou[3], and Jian-Guo Dai[4]*

1. Research Assistant Professor, Department of Civil and Environmental Engineering, The Hong Kong Polytechnic University, Hong Kong. Email: mingfeng.kai@polyu.edu.hk, ORCID: 0000-0002-7626-2328
2. Professor, Department of Civil and Environmental Engineering, Vanderbilt University, Nashville, TN, USA. Email: florence.sanchez@vanderbilt.edu, ORCID: 0000-0002-1176-2751
3. Professor, Department of Civil Engineering, Qingdao University of Technology, Qingdao, China. Email: dshou@outlook.com, ORCID: 0000-0002-1252-2987
4. Professor (Corresponding author), Department of Civil and Environmental Engineering, The Hong Kong Polytechnic University, Hong Kong. Email: cejgdai@polyu.edu.hk, ORCID: 0000-0001-9904-7914

Abstract

The interfacial characteristics between cement paste and silica are far from being fully understood, especially from the nanoscale perspective. Herein, molecular models were used to provide comprehensive insights into the interfacial characteristics between calcium silicate hydrate (C-S-H, the main binding phase of cement paste) and silica. Chemically, various types of bonds existed at the interface, including H-bonds and Ca−O bonds, and proton (H^+) exchange occurred between C-S-H and silica. An increase in the water content of C-S-H could depress the deprotonation of the Si-OH groups on the silica surface. Structurally, an atomic-level interfacial transition zone (ITZ) with a low density was identified, which was attributed to the rich presence of –OH groups at the C-S-H–silica interface. The water molecules and calcium ions in the ITZ diffused faster than those in the bulk C-S-H. Mechanically, the interfacial bond strength was inversely related to the water content of C-S-H, with the higher water content reducing the interfacial interactions. Under loading, the interfacial fracture underwent three stages: crack propagation, atomic chain bridging (responsible for the interfacial residual strength), and complete failure. These atomic-level findings provide hitherto unknown mechanisms of the interfacial interactions between cement paste and silica.

Keywords: Interfacial bonding; Proton exchange; Interfacial transition zone; Bond strength; Interfacial fracture

1. Introduction

Concrete, composed of fine and coarse aggregates bonded together by hydrated cement, is one of the most consumed building materials. However, the concrete production brings forth noteworthy environmental burdens, contributing to 7–10% of the global human-made CO_2 emissions [1, 2]. Besides, buildings constructed with concrete may confront structural vulnerability due to the low tensile strength of concrete, leading to unignorable safety issues. To reduce the environmental footprint and address the safety concerns, the concept of introducing additional materials from the nano- to macro-scale has been advocated to enhance the performance of concrete over the past decades. Among these materials, silica of varied forms, including nano-silica particles [3], silica fume [3], glass fiber [4], silica-coated fiber [5], and so on, is one of the most commonly used materials to improve the mechanical properties of concrete. However, the reinforcing efficiency of silica is strongly dependent on the interfacial characteristics between cement paste and silica [6-8].

To date, many experimental studies have been carried out to unravel the interfacial interactions between cement paste and silica of varied forms. For nano-silica and silica fume, they could serve as nanofillers between the gel particles of calcium silicate hydrates (C-S-H, the main binding phase of hydrated cement) [9, 10]. Besides, nano-silica and silica fume could also facilitate the formation of C-S-H gel and densify the matrix through reactions with calcium hydroxide (the secondary hydrates in cement paste) [9, 10]. For fibrous silica (e.g., glass fiber), the Ca/Si ratio was lower at the matrix-fiber interface with respect to that of the matrix [7]. In addition, the interfacial strength between cement matrix and glass fiber clearly increases with the decrease in the water/cement (w/c) ratio of the matrix [7]. For larger-scale silica (e.g., silica sand), its interface with the matrix usually has a low density, as observed by backscattered electron imaging, by virtue of the so-called “wall effect” [11-13]. In contrast to the matrix-fiber interface, the Ca/Si ratio at the matrix-silica sand interface is higher than that of the matrix due to the richness of portlandite in the interfacial transition zone (ITZ). Undoubtedly, the roles of different silica structures in the cement paste could vary with each other. However, a common principle shared by these silica structures is that the interfacial nature between cement paste and

silica plays a vital role in altering the performance of cement matrix. The interfacial strength can be affected by many factors, such as the chemical composition of cement, the type, shape and surface texture of silica, the curing age, and temperature [13-16]. Despite this, many interfacial features, especially at the nanoscale level, still remain somewhat an enigma due to the complexity of the interfacial microstructure and the constraints imposed by existing experimental techniques [17].

Molecular dynamics (MD), a tool for analyzing the movements of atoms and molecules, can provide direct nanoscale insight into the chemical and physical basis of materials [18, 19]. Most of the classical MD use empirical interatomic potentials with predefined functional forms to capture the chemistry and physics of materials. To incorporate flexibility in the functional form, the machine learning approach shows marked success in developing interatomic potentials for a wide range of materials (e.g., two-dimensional (2D) materials, metals and oxides) [20, 21]. In 2009, Pellenq et al. [22] developed a tobermorite-like C-S-H model with a stoichiometry of $(CaO)_{1.65}(SiO_2)(H_2O)_{1.75}$. Following this model building procedure, many studies have been carried out to investigate the mechanical, fracture, thermal, and transport properties of cement paste at the molecular level [23-30] . Recently, some amorphous C-S-H molecular models have also been developed, which shed atomic-level lights on the understanding of structural characteristics, elastic deformation, hydration mechanisms, silicate chain growth in cement paste, and the growth of amorphous C-S-H gel on substrates [31-35]. In addition, the MD tool has been widely applied to study the interfacial properties in many composite systems. For example, Kai et al. [36] studied the interfacial chemical events and mechanical behaviors between geopolymer and silica, focusing on the influence of the Si/Al ratio of geopolymer. Sun et al. [37] performed MD simulation of the interactions of amine molecules with C-S-H substrates in an aqueous environment. Other interfacial structures, such as C-S-H−geopolymer [38], water−silica [39], polymer−silica [40], polymer−metal [41], and graphene−polymer [42], were also investigated. These studies led to a better understanding of the interfacial physics and chemistry in different composites, which are often not accessible experimentally. In addition, the atomic-level properties obtained from atomistic simulation can

provide essential information for the multiscale investigation, which is beneficial for understanding the material performance from the nanoscale to macroscale [43, 44]. To the best of the authors' knowledge, however, only a few MD studies have been carried out on the interfacial characteristics between cement paste and silica. Zhou et al. [45] constructed a C-S-H–silica model to reveal the interfacial behaviors between cement paste and silica, but the surface structure (Si-O^-) of the silica model did not consist with the fact that the silica surface is in the hydrated form (Si-OH) [46, 47]. Therefore, it calls for a comprehensive molecular-level investigation of the interaction mechanisms at the C-S-H–silica interface.

In this work, molecular models of C-S-H–silica systems were developed to elucidate the interfacial characteristics from the nanoscale perspective. First, the interfacial interaction mechanisms between C-S-H and silica were studied, and the interfacial structures were characterized. Then, the atom trajectories were recorded to analyze the diffusion behavior of the water (H_2O) molecules and calcium (Ca^{2+}) ions of the C-S-H molecular structure at the silica surface. Finally, the bond strength between C-S-H and silica was determined and the full-range fracture process at the interface was captured. In addition, the water content of C-S-H, an important factor that affects interfacial characteristics, was considered. The atomic-level information provided in this work can reveal unknown mechanisms underlying the interfacial interactions between cement paste and silica and be used to derive the essential interaction parameters for the multiscale simulation of cement paste-silica interface.

2. Simulation Method

2.1 Model construction

To start, a quartz-alpha unit was selected as the building block structure for the silica model [48-50], as shown in Fig. 1(a). This unit is a monoclinic cell with a size of a = 5.402 Å, b = 4.91 Å, c = 4.91 Å ($\alpha = 120^o$, $\beta = \gamma = 90^o$). To construct the silica substrate, a (7 × 8 × 10) supercell of the unit was converted into an orthorhombic configuration with a size of 37.81 Å × 39.28 Å × 42.52 Å (Fig. 1a) [51]. Next, two exposed silica surfaces were created by assigning hydrogen (H) atoms to the exposed oxygen (O) atoms on the upper and lower surfaces to produce a

hydrated form (Si-OH) at the surfaces (Fig. 1a), in agreement with the experimental observation that silicon (Si) atoms usually exist in the hydrated form at the silica surface [46, 47]. Please note that for some real silica materials (e.g., nano-silica and silica fume), their molecular structures prefer to be amorphous [46, 47], but it is not necessary to transform the crystalline silica model into an amorphous one as the interfacial nature between two phases is determined by the surface chemistry [52]. Next, amorphous C-S-H molecular models with various water contents were created and placed in contact with the surface of the silica model. The C-S-H molecular structures were composed of the silicate chains (including 12 monomers, 30 dimers, 8 pentamers, and 2 octamers), 218 Ca^{2+} ions resulting in a Ca/Si ratio of 1.7 [22], and 38 O^{2-} ions (for charge balance [22]), as well as different numbers of H_2O molecules (for representing various water contents). The H_2O/Si ratio of these C-S-H structures ranged from 1.0 to 3.0, which was within the range (1.0−4.0) obtained from experiments reported in the literature [53]. The silicate chain length followed the 3n-1 rule [54], and the silicate chains had a Q_n distribution (Q_0 = 9%, Q_1 = 63% and Q_2 = 28%) that was close to that of experimental samples (Q_0 =10%, Q_1 = 67% and Q_2 = 23%) [55]. These silicate chains, ions, and H_2O molecules were randomly packed into the empty space at the silica surface to construct the initial amorphous C-S-H molecular structures, as done in Ref. [56]. The empty space increased gradually from 40 Å to 50 Å in height when the H_2O/Si ratio ranged from 1.0 to 3.0. Fig 1 (b) shows three molecular models of the C-S-H−silica systems with H_2O/Si ratios of 1.0, 2.0 and 3.0.

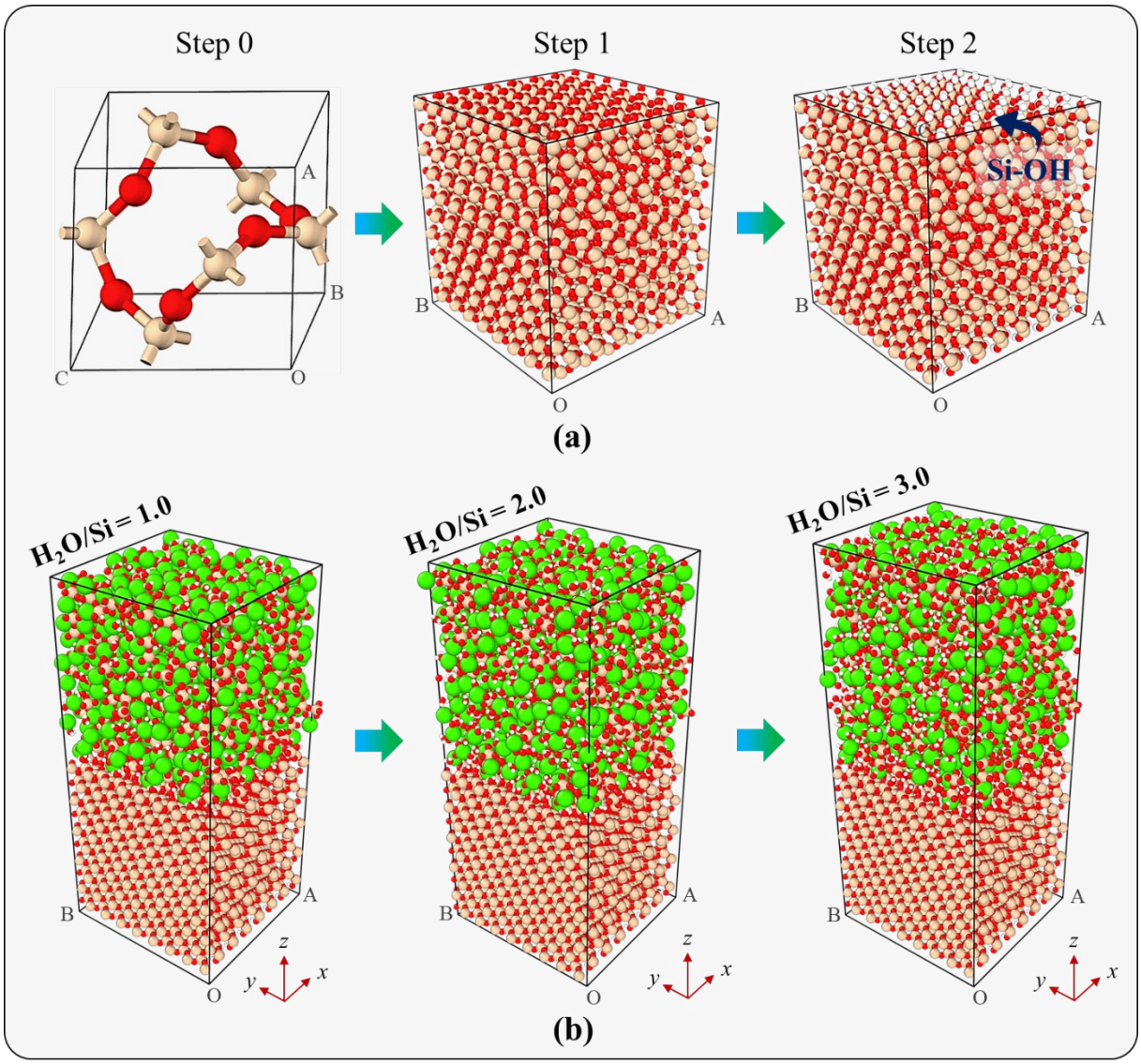

Fig. 1 (a) Procedure to prepare the atomic model of silica: Step 0: SiO_2-alpha unit cell; Step 1: orthorhombic configuration of the silica; Step 2: final molecular model of silica with the surfaces in hydrated form; and (b) Perspective views of the molecular models of C-S-H−silica systems with a H_2O/Si ratio of 1.0, 2.0, and 3.0, respectively. (Yellow spheres denote the Si atoms; Red spheres denote the O atoms; White spheres denote the H atoms; Green spheres denote the Ca atoms.)

2.2 Simulation procedure

First, the initial molecular models were geometry-optimized by performing an energy minimization of the systems via the conjugate gradient (CG) algorithm with a convergence criterion of 10^{-6} kcal/mol for energy and 10^{-6} kcal/mol-Å for force, followed by thermodynamic

equilibrium that was carried out for 500 ps in an isothermal-isobaric (NPT) ensemble with a temperature of 500 K and a pressure of 101 kPa (atmospheric pressure). The Berendsen thermostat and barostat algorithms were applied for the temperature and pressure control [57]. This thermal treatment accelerated the chemical and physical events in the interfacial structures to reach the equilibrium state. During this process, some H_2O molecules of the C-S-H dissociated into OH^- and H^+ ions [58, 59]. The OH^- ions predominantly reacted with the Ca^{2+} ions of the C-S-H to form Ca–OH bonds, while the H^+ ions were adsorbed by the silicate chains to transform the Si-O^- into the Si-OH groups. After thermal treatment, the systems were cooled down to 300 K (room temperature) with a cooling rate of 10 K/ps. Subsequently, the systems were further equilibrated for an additional 300 ps in an NPT ensemble with a temperature of 300 K and a pressure of 101 kPa.

A series of analyses was then performed on these C-S-H–silica molecular models. First, the interfacial interaction between C-S-H and silica was investigated at the equilibrium states by determining the interfacial bonding. Next, the density fields of these molecular models were analyzed to further understand the structural characteristics of the C-S-H–silica systems. To study the diffusion characteristics of the H_2O molecules (including dissociated H_2O, namely OH^- ions) and Ca^{2+} ions in the C-S-H structures, the atom trajectories of the H_2O molecules and Ca^{2+} ions were recorded by further equilibrating these systems for 200 ps in a canonical (NVT) ensemble with a temperature of 300 K. To investigate the interfacial mechanical properties and fracture characteristics of these C-S-H–silica molecular models, a uniaxial tensile load was applied on the structures along the z-direction (perpendicular to the interface). The load scheme was carried out by fixing the lower regions (z coordinate smaller than 5.0 Å) and then assigning a constant velocity (0.0001 Å/ps) to the upper regions (z coordinate larger than 80.0 Å). The tensile velocity employed in this study was in the range widely suggested in the literature for MD simulation of uniaxial tensile loading [36, 60]. During the tensile loading, the Berendsen thermostat (300 K) was employed to control the temperature of the middle regions that were subject to tension.

All the simulations were performed using the Large-scale Atomic/Molecular Massively

Parallel Simulator (LAMMPS) package. The simulation timestep was set to 0.25 fs, and periodic boundary conditions (PBCs) were applied to all directions (x, y, and z) of the molecular models for all simulations.

2.3 Reactive force field

In this study, the reactive force field (ReaxFF), originally developed by Adri van Duin et al. [61], was adopted to describe both inter- and intra-molecular interactions in the systems. The ReaxFF is a bond order-based force field that is able to deal with both chemical (i.e., bond formation and dissociation) and physical events in materials. In this force field, the total potential energy is a sum of various partial contributions given by the equation,

$$E_{Total} = E_{bond} + E_{angle} + E_{tor} + E_{over} + E_{under} + E_{lp} + E_{H\text{-}bond} + E_{vdW} + E_{coul} \quad (1)$$

where E_{bond}, E_{val} and E_{tor} represent bond energy, valence angle energy, and torsion angle energy, respectively; E_{over} and E_{under} are over-coordination energy penalty and under-coordination stability, respectively; E_{lp} is a lone-pair energy based on the number of lone pairs around an atom; $E_{H\text{-}bond}$, E_{vdW} and E_{coul} represent hydrogen-bond (H-bond) energy, van der Waals energy, and Coulomb energy, respectively. The atomic charges were adjusted at each MD timestep using the Charge equilibration (QEq) scheme. A more detailed description of these energy terms in the ReaxFF can be found elsewhere [62].

In this study, the ReaxFF parameter set was obtained from Ref. [63], which was developed by Adri van Duin's group and have benchmarked against high-level quantum mechanics (QM) calculations of Ca/Si/O/H systems via a successive one-parameter search technique to minimize the error [62]. This parameter set has already been successfully applied to study a variety of materials, such as calcium hydroxide ($Ca(OH)_2$) [64], silica [65], and C-S-H gel [55]. Based on the radial distribution function (RDF) analysis, the bond length for various bond types in the C-S-H and silica was obtained, as shown in Table 1. The values agreed well with the DFT results from the literature, indicating that the ReaxFF used in this study can well model the molecular structures.

Table 1 The average bond length of various bond types in the C-S-H and silica models based on the RDF analysis

Bond type	C-S-H		Silica	
	This work	From literature	This work	From literature
Ca-O bond	2.52 Å	2.5 Å [66]	–	–
Si-O bond	1.56 Å	1.6 Å [66]	1.59 Å	1.61 Å [67]
O-H bond	0.97 Å	0.97 Å [68]	0.99 Å	0.98 Å [69]
H-bond	2.45 Å	2.37 Å [70]	–	–

3. Results and Discussion

3.1 Interfacial interactions

Interfacial interactions are an important material characteristic that plays a key role in the properties of various composites. By studying the C-S-H−silica systems at the equilibrium state, different types of interfacial bonds could be identified, as shown in Fig. 2(a). The silicate chains of the C-S-H structure (Fig. 2a.1) could interact with the silica via H-bonds (defined as type 1 H-bonds). The interfacial H-bond could be formed (1) between two Si-OH groups, one of which donated the H atom while the other provided the O atom to accept the H atom, or (2) between one Si-OH group that donated the H atom and one Si-O^- group that accepted the H atom. Similarly, the H_2O molecules (or OH^- ions) of the C-S-H structure (Fig. 2a.2) could also interact with the silica via H-bonds (defined as type 2 H-bonds) by either donating or accepting the H atoms. Moreover, they could also interact with the silicate chains of the C-S-H structure via H-bonds, which could be viewed as the link between the silicate backbone of the C-S-H structure and the silica. The Ca^{2+} ions of C-S-H structure (Fig. 2a.3) could interact with the silica via Ca−O ionic bonds. The interfacial Ca−O bond number per Ca^{2+} ion ranged from 1 to 4. At the same time, they could also interact with the silicates of the C-S-H structure via Ca−O ionic bonds, which could also be viewed as the link between the silicate backbone of the C-S-H structure and the silica. In addition, the H-bond number (type 1 and 2) and Ca−O bond number between the C-S-H structure and the silica were counted for all structures with H_2O/Si ratio ranging from 1.0 to 3.0, as shown in Fig. 2(b). The interfacial H-bond number (type 1 and 2) increased while the interfacial Ca−O bond number decreased with increasing H_2O/Si molar

ratio. For all interfaces, the H-bond number was much more than the Ca−O bond number for H_2O/Si ratio ranging from 1.0−3.0. In conclusion, the C-S-H molecular structures interacted with the silica via H-bonds (type 1 and 2) and Ca−O ionic bonds. H-bond was the dominant bond type at the interface. Increasing the water content of C-S-H led to more H-bonds (type 1 and 2), but reduced the Ca−O ionic bonds at the interface.

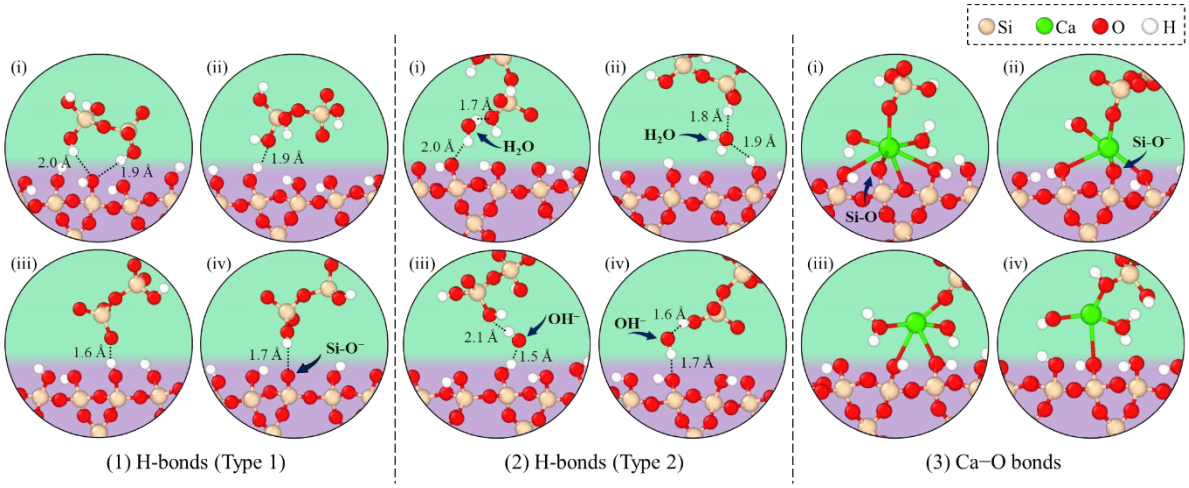

(a) Snapshots of the different interfacial bond schemes

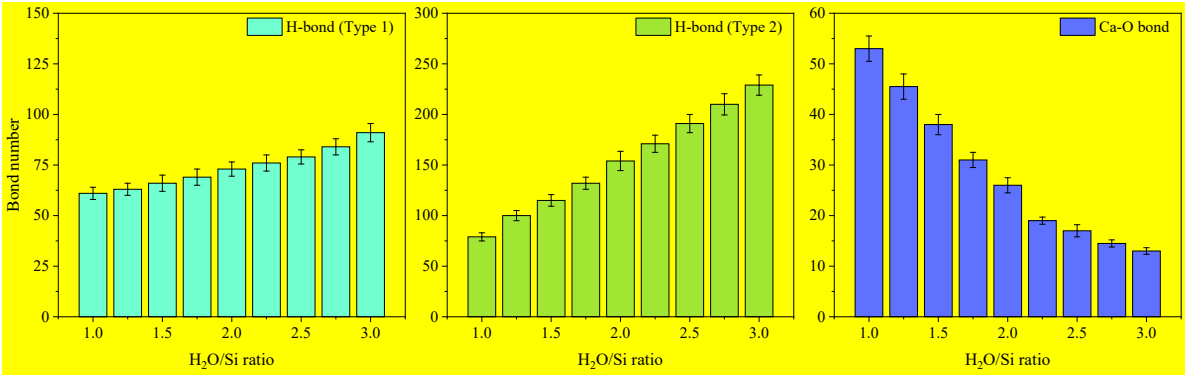

(b) Interfacial bond numbers

Fig. 2 (a) Snapshots of the interfacial bonds between C-S-H and silica: (a.1) Type 1 H-bonds representing bonding between the silicate chains of C-S-H and silica; (a.2) type 2 H-bonds representing bonding between H_2O (or OH^-) of C-S-H and silica; (a.3) Ca–O ionic bonds between Ca^{2+} ions of C-S-H and silica; and (b) Interfacial bond number between C-S-H and silica, including type 1 H-bonds, type 2 H-bonds, and Ca–O bonds.

Interestingly, it was found that there were some chemical events between C-S-H and silica due to proton (H^+) transfer among the interfacial components. Two chemical reaction pathways

could be concluded from the chemical events at the interface, as exhibited in Fig. 3(a). For pathway 1 (the main reaction pathway), the OH^- ions that dissociated from the H_2O molecules could take the H^+ from the Si-OH groups at the silica surface, which transformed the OH^- ions into H_2O molecules and the Si-OH groups into $Si\text{-}O^-$ groups. The $Si\text{-}O^-$ groups on the silica surface could further take the H^+ from the H_2O molecules of the C-S-H, which transformed the H_2O molecules into OH^- ions and the $Si\text{-}O^-$ groups back to Si-OH groups. For pathway 2 (occasional reaction pathway), a few $Si\text{-}O^-$ groups of the silicates in the C-S-H could directly take the H^+ from the Si-OH groups at the silica surface, and these H^+ could also be taken back by the new $Si\text{-}O^-$ groups at the silica surface. During the reaction process, more H^+ were transferred from the silica surface to C-S-H, resulting in some $Si\text{-}O^-$ groups that could be observed on the silica surface at the equilibrium state, which is counted in Fig. 3(b). The results demonstrated that increasing the H_2O/Si ratio of the C-S-H can reduce deprotonation of the Si-OH groups at the silica surface. Deprotonation of silica is a common characteristic in alkaline environment as the ≡Si-OH groups possess weak acidity [71]. In conclusion, there existed H^+ exchange between C-S-H and silica through two reaction pathways: one was the H^+ transfer from the Si-OH groups of silica to the OH^- in the C-S-H and then from the H_2O in C-S-H to the $Si\text{-}O^-$ groups of silica; the other pathway was the H^+ transfer between the Si-OH groups of silica and the $Si\text{-}O^-$ groups of C-S-H. Moreover, less Si-OH groups were deprotonated from the silica surface with increasing water content of the C-S-H.

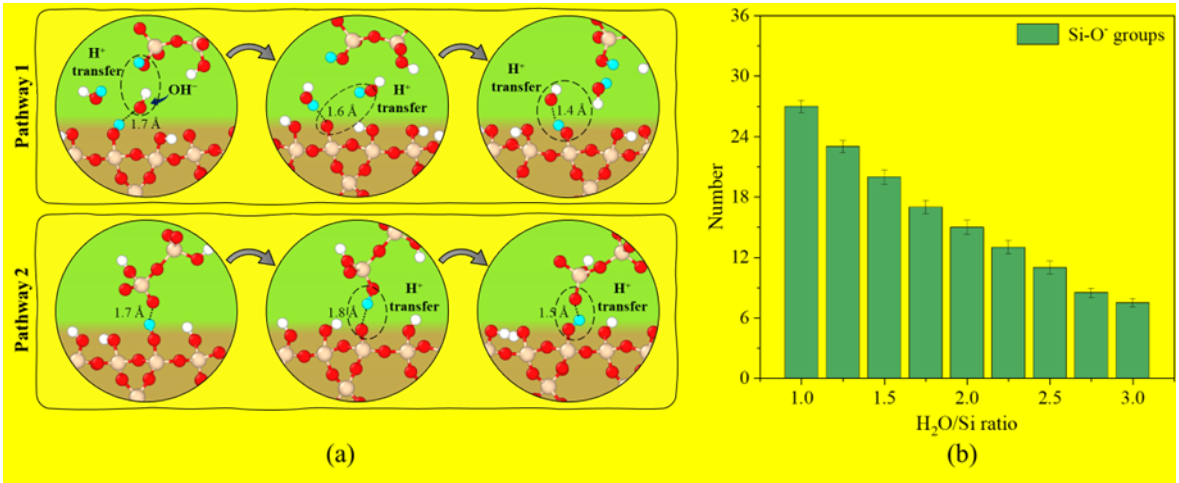

Fig. 3 (a) The two chemical reaction pathways between C-S-H and silica. The atoms labeled in blue color represent the H^+ involved in the reaction process; and (b) Number of Si-O^- groups on the silica surface as a function of the H_2O/Si ratio of C-S-H.

3.2 Interfacial transition zone

The atomic structures of the C-S-H−silica model systems were characterized by calculating the density field. Fig. 4(a−c) presents three density fields of the systems with a H_2O/Si ratio of 1.0, 2.0 and 3.0. By analyzing the density distribution based on colors, it could be found that the C-S-H−silica interface had a relative lower density than the bulk C-S-H, which could be defined as an atomic-level ITZ [36]. The formation mechanism of this ITZ could be attributed to the rich presence of –OH groups at the interface provided by both the C-S-H (Si-OH, H_2O and OH^-) and the silica (Si-OH). As shown in Fig. 2 (a) and (b), the interfacial interactions were dominated by H-bonds, which generated a density field approaching that of water (1 g/cm^3 for a complete H-bond system). To further understand the ITZ features and the effect of C-S-H water content, the mass density profile of the three C-S-H–silica model systems (H_2O/Si ratio = 1.0, 2.0 and 3.0) was plotted in Fig. 4(b) as a function of distance along the z-direction. The ITZ widths of these systems were 3.20 Å, 3.35 Å, and 3.40 Å, respectively, which indicated a slight increase (~ 6%) of the width with the H_2O/Si ratio. The ITZ density were 1.12 g/cm^3, 1.06 g/cm^3, and 0.99 g/cm^3, respectively, suggesting that the ITZ density can decrease gradually when the H_2O/Si ratio of C-S-H increases as a result of more –OH groups concentrating at the interface. Atomic-level ITZ of low density has been previously reported at the interface of various composites, such as the SiO_2−epoxy interface [72], the SiO_2−geopolymer interface [36], and the carbon nitride−epoxy interface [73]. In conclusion, the results evidenced the presence of an atomic-level ITZ of low density between C-S-H and silica. Increasing the water content of C-S-H led to an increase of the ITZ width but a decrease of the ITZ density.

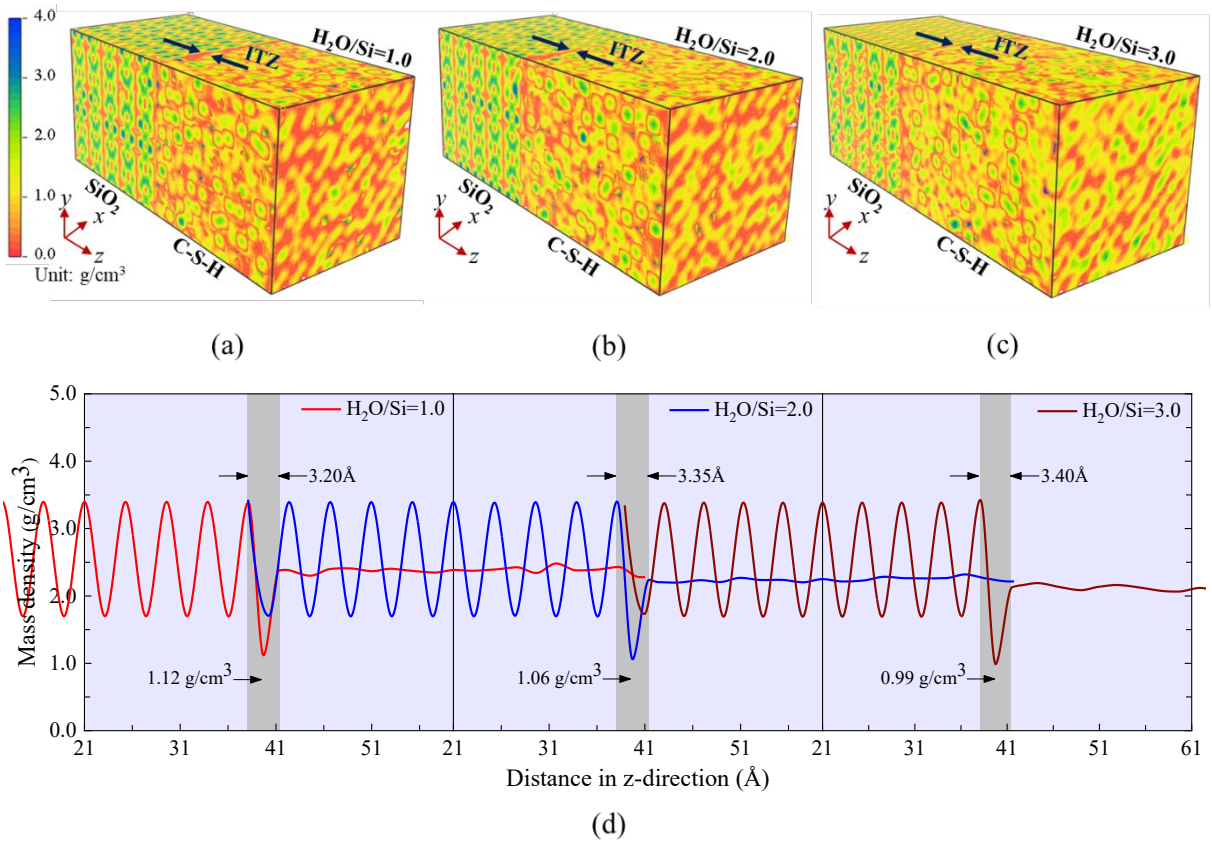

Fig. 4 (a–c) Density fields of the C-S-H–silica systems with a H_2O/Si ratio of 1.0, 2.0 and 3.0. In this study, PBCs were employed for all systems, so there was another ITZ at the boundary, which is not labeled; and (d) Mass density profiles of the three C-S-H–silica model systems (H_2O/Si ratio of 1.0, 2.0 and 3.0) as a function of the distance along z-direction.

Next, the diffusion behavior of the H_2O molecules (including OH^- ions) and Ca^{2+} ions in the ITZ was characterized. To assess the diffusion behavior, the mean squared displacement (MSD), a measure of the deviation of the position of an atom with respect to its reference position over time, was computed over a timescale of 200 ps using the following equation:

$$MSD(t) = \langle |\boldsymbol{r}(t) - \boldsymbol{r_0}|^2 \rangle = \frac{1}{N}\sum_{i=1}^{N} |\boldsymbol{r}_i(t) - \boldsymbol{r}_i(0)|^2 \quad (1)$$

where N is the atom number to be averaged; $\boldsymbol{r}_i(t)$ and $\boldsymbol{r}_i(0)$ are the position of the i-th atom at time and t and 0 (the reference position). Fig. 5 summarizes the MSD values of the H_2O molecules and Ca^{2+} ions in the ITZ of the three C-S-H–silica model systems with a H_2O/Si ratio of 1.0, 2.0 and 3.0. For reference, the MSD values of the H_2O molecules and Ca^{2+} ions in the

bulk C-S-H (as taken from the middle 10 Å-thick zone of the C-S-H structures) were also calculated. Overall, the MSD values of the H_2O molecules and Ca^{2+} ions in both the ITZ and bulk C-S-H increased over time, which was indicative of the diffusion process. For all structures, the MSD values of the H_2O molecules and Ca^{2+} ions in the ITZ were higher than those in the bulk C-S-H. Moreover, the MSD values of the H_2O molecules and Ca^{2+} ions in the ITZ became larger as the H_2O/Si ratio of the C-S-H increased. Therefore, it can be concluded that the H_2O molecules and Ca^{2+} ions diffused faster in the ITZ than in the bulk C-S-H. Furthermore, increasing the water content of C-S-H accelerated the diffusion of the H_2O molecules and Ca^{2+} ions in the ITZ.

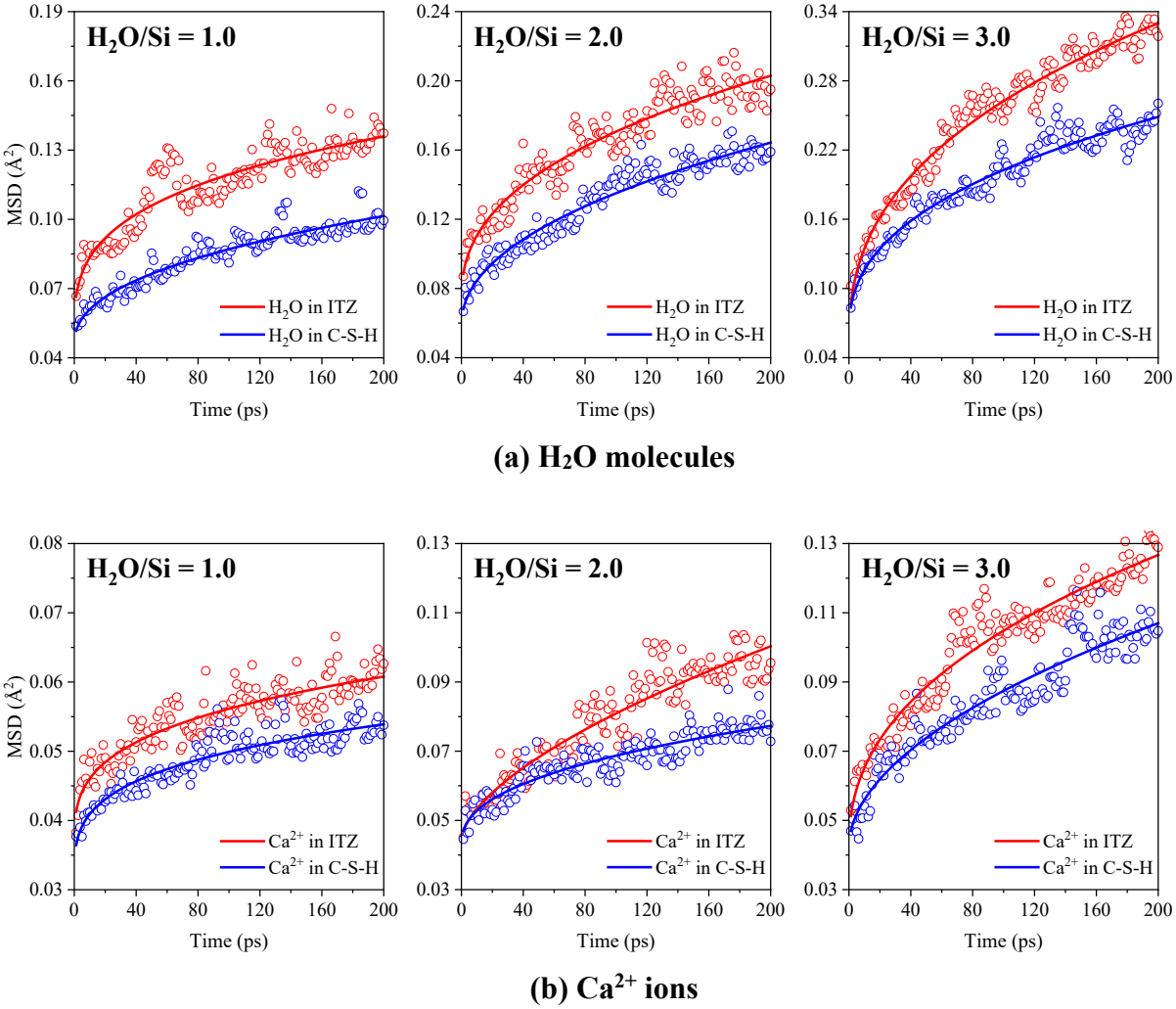

Fig. 5 (a) MSD values of the H_2O molecules in the ITZ and bulk C-S-H (H_2O/Si ratio = 1.0, 2.0 and 3.0); (b) MSD values of the Ca^{2+} ions in the ITZ and bulk C-S-H (H_2O/Si ratio = 1.0, 2.0 and 3.0). According to the overall trend of the MSD values, the linear logarithmic transform function ($y = a + bx\hat{}c$) was employed to fit the data.

3.3 Interfacial bond strength

The interfacial bond strength between C-S-H and silica is one of the most significant features that plays a key role in concrete performance. A series of tension tests was carried out on the C-S-H−silica model systems to investigate the interfacial bond strength. Fig. 6(a) illustrates the loading scheme that fixes 5Å-thick silica atoms at the bottom and then applies a pull force on the upper C-S-H atoms, leaving 75Å-thick structures to deform. During the tensile process, the pull force−displacement curves were plotted, as shown in Fig. 6(b). For all model systems, the pull force increased linearly with the pull displacement (elastic stage) and then reached a peak, after which the pull force decreased gradually (fracture stage). The peak load was 39.6 nN, 31.9 nN, and 25.2 nN, respectively for the three systems with a H_2O/Si ratio of 1.0, 2.0 and 3.0, corresponding to an interfacial bond strength of 2.56 GPa, 2.08 GPa, and 1.63 GPa, respectively. These results demonstrated that the bond strength between C-S-H and silica was reduced by increasing the H_2O/Si ratio of the C-S-H. At the fracture stage, the pull force existed over a long range, suggesting that the C-S-H−silica systems sustained a residual strength under a large tensile deformation until reaching the failure point. The interfacial residual strength of the three systems at a given strain followed the following order: H_2O/Si ratio = 1.0 > H_2O/Si ratio = 2.0 > H_2O/Si ratio = 3.0. In contrast, the occurrence of the failure point followed a different order: H_2O/Si ratio = 1.0 > H_2O/Si ratio = 3.0 > H_2O/Si ratio = 2.0, which indicated that the C-S-H−silica systems with the H_2O/Si ratio of 2.0 could resist the largest tensile deformation before reaching the failure point. In conclusion, the interfacial bond strength and residual strength between C-S-H and silica were inversely related to the water content of C-S-H. The C-S-H−silica systems sustained a long-range residual strength until reaching the failure point, which occurred in the following order: H_2O/Si ratio = 1.0 > H_2O/Si ratio = 3.0 > H_2O/Si ratio = 2.0.

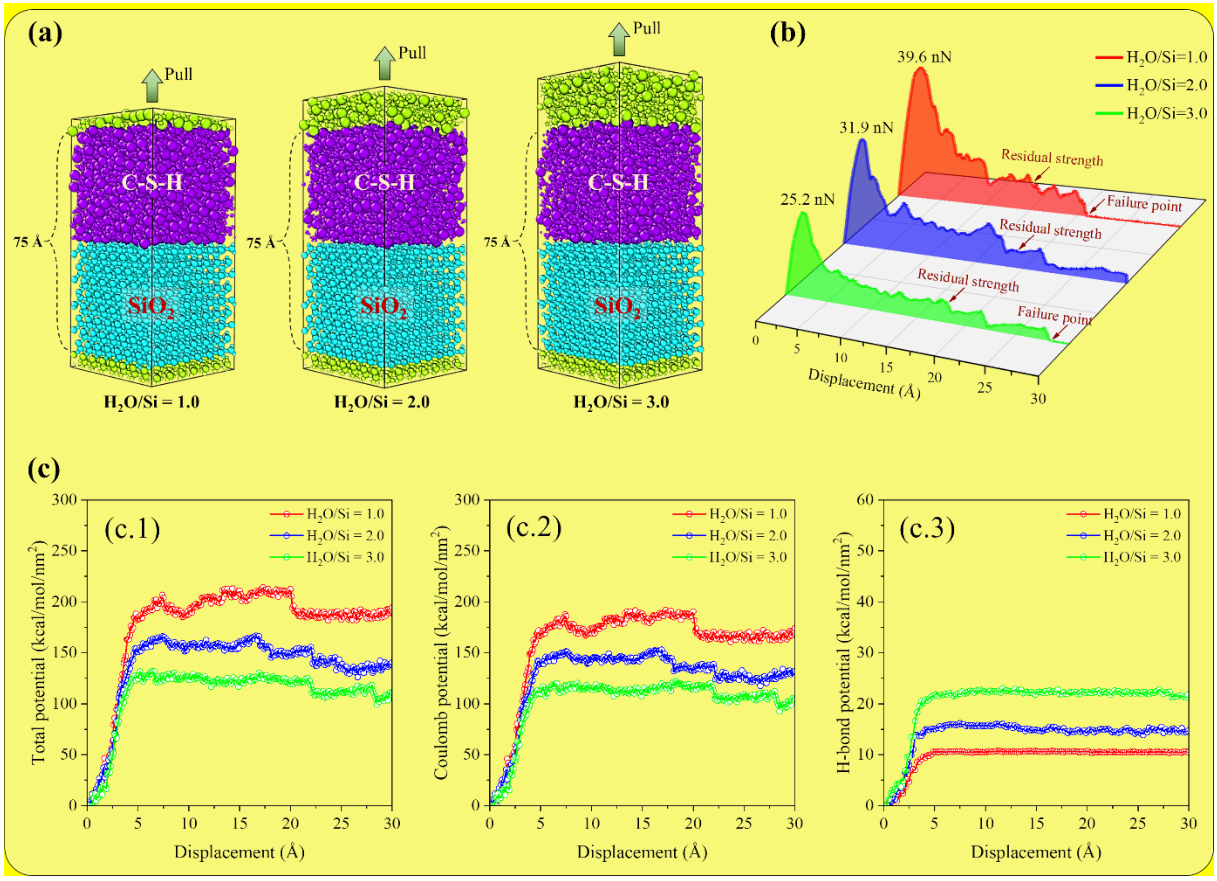

Fig. 6 (a) Loading scheme performed on the C-S-H–silica model systems with a H_2O/Si ratio of 1.0, 2.0 and 3.0. A 5 Å-thick layer of silica atoms at the bottom (green color) was fixed while the upper atoms (green color) with z coordinates > 80 Å were subjected to a pull force. As a result, all model systems had a 75 Å-thick structure (represented in purple color for the C-S-H atoms and in blue color for the silica atoms) that could deform under the pull force; (b) Pull force–displacement curves of the C-S-H–silica model systems with a H_2O/Si ratio of 1.0, 2.0 and 3.0; and (c) Variation of the interfacial total potential, coulomb potential, and H-bond potential as a function of the pull displacement.

To further understand the interfacial bond properties, the variation of the interfacial potential was calculated during the tensile process using the following equation:

$$E_{Interface} = E_{System} - E_{C-S-H} - E_{Aggregate} \quad (2)$$

where E_{System} is the system potential of the C-S-H–silica model systems; E_{C-S-H} is the potential of C-S-H, and $E_{Aggregate}$ is the potential of silica. Fig. 6(c.1) shows the variation of the total interfacial potential of the three C-S-H–silica systems with a H_2O/Si ratio of 1.0, 2.0

and 3.0 as a function of the pull displacement. For all systems, the total interfacial potential increased with the pull displacement, and then reached a plateau, at which stage the total interfacial potential fluctuated over a small range. The maximum increase of the total interfacial potential was 212.6 kcal/mol/nm^2, 166.2 kcal/mol/nm^2, and 132.3 kcal/mol/nm^2, respectively for the three systems (H_2O/Si ratio = 1.0, 2.0, and 3.0), respectively. These results indicated that increasing the water content of C-S-H reduced the interfacial energy consumption during the tensile process. Since the variation of interfacial potential corresponds to the loss of interfacial interactions, it was concluded that the interfacial interaction between C-S-H and silica was weakened by increasing the water content of C-S-H.

To explain how the water content of C-S-H affected the interfacial interaction between C-S-H and silica, two key contributions to the total interfacial potential, including the interfacial Coulomb potential and H-bond potential, were calculated, as shown in Fig. 6(c.2) and (c.3). It should be noted that the interfacial van der Waals (vdW) potential is not discussed here because this potential did not increase during the tensile process, which indicated that its contribution to the interfacial bond strength could be ignored. The variation of the interfacial Coulomb potential almost followed the same trend as that of the total interfacial potential, which demonstrated that the interfacial Coulomb potential was the main contributor of the interfacial interaction. Increasing the H_2O/Si ratio of the C-S-H reduced the interfacial Coulomb potential. During the tensile process, the maximum increase of the interfacial H-bond potential was 10.68 kcal/mol/nm^2, 16.18 kcal/mol/nm^2, and 22.77 kcal/mol/nm^2, respectively for the three C-S-H−silica systems (H_2O/Si ratio = 1.0, 2.0 and 3.0), suggesting that increasing the H_2O/Si ratio of the C-S-H enhanced the interfacial H-bond potential, but that its contribution to the interfacial interactions was very small. It could, therefore, be concluded that increasing the water content in C-S-H reduced the interfacial Coulomb potential (the main contributor of the interfacial interaction), leading to a weakened interface, despite the fact that the interfacial H-bond interaction (a small contributor of the interfacial interaction) was enhanced. These results further explain why higher water content of C-S-H can weaken the interfacial interaction between C-S-H and silica.

3.4 Fracture properties

Snapshots of the C-S-H−silica systems were captured during the tensile loading to provide insight into their fracture process, as shown in Fig. 7. Overall, the fracture process of the structures underwent three stages: crack propagation, atomic chain bridging through the C-S-H atoms (Ca^{2+} ions, OH^- ions, H_2O molecules, and short silicate chains), and complete failure (breakage of all atomic chains). The cracks always propagated at the interface between C-S-H and silica, which indicated that the interface was relatively weak compared to bulk C-S-H and silica. For all structures, the cracks propagated very quickly, and large cracks were easily observed at the interface when the pull displacement reached 5.0 Å. A long-range atomic chain bridging process could then be observed, which involved the simultaneous gradual growth and loss of the atomic chains. For example, for the pull displacement ranging from 5.0 Å to 20.0 Å (Fig. 7a; H_2O/Si ratio = 1.0), the atomic chains between C-S-H and silica grew gradually while at the same time the partial atomic chains ruptured during the tensile process. The main difference among the systems with a H_2O/Si ratio of 1.0, 2.0 and 3.0 was that their atomic chain bridging process lasted for different displacements, ~22.5 Å, ~35.0 Å, and ~30.0 Å, respectively. After reaching complete failure, a few C-S-H atoms were found on the silica surface. By comparing Fig.6(b) with Fig. 7, it can be seen that the failure point of the structures at which the residual bond strength dropped to 0 corresponded to a displacement where the last atomic chain broke. These results indicated that the residual strength of the structures under tensile loading was attributed to atomic chain bridging. In summary, atomic chain bridging was responsible for the residual strength of the C-S-H−silica systems during tensile loading, which is why the breakage of the last atomic chain led to the complete loss of the interfacial bond strength.

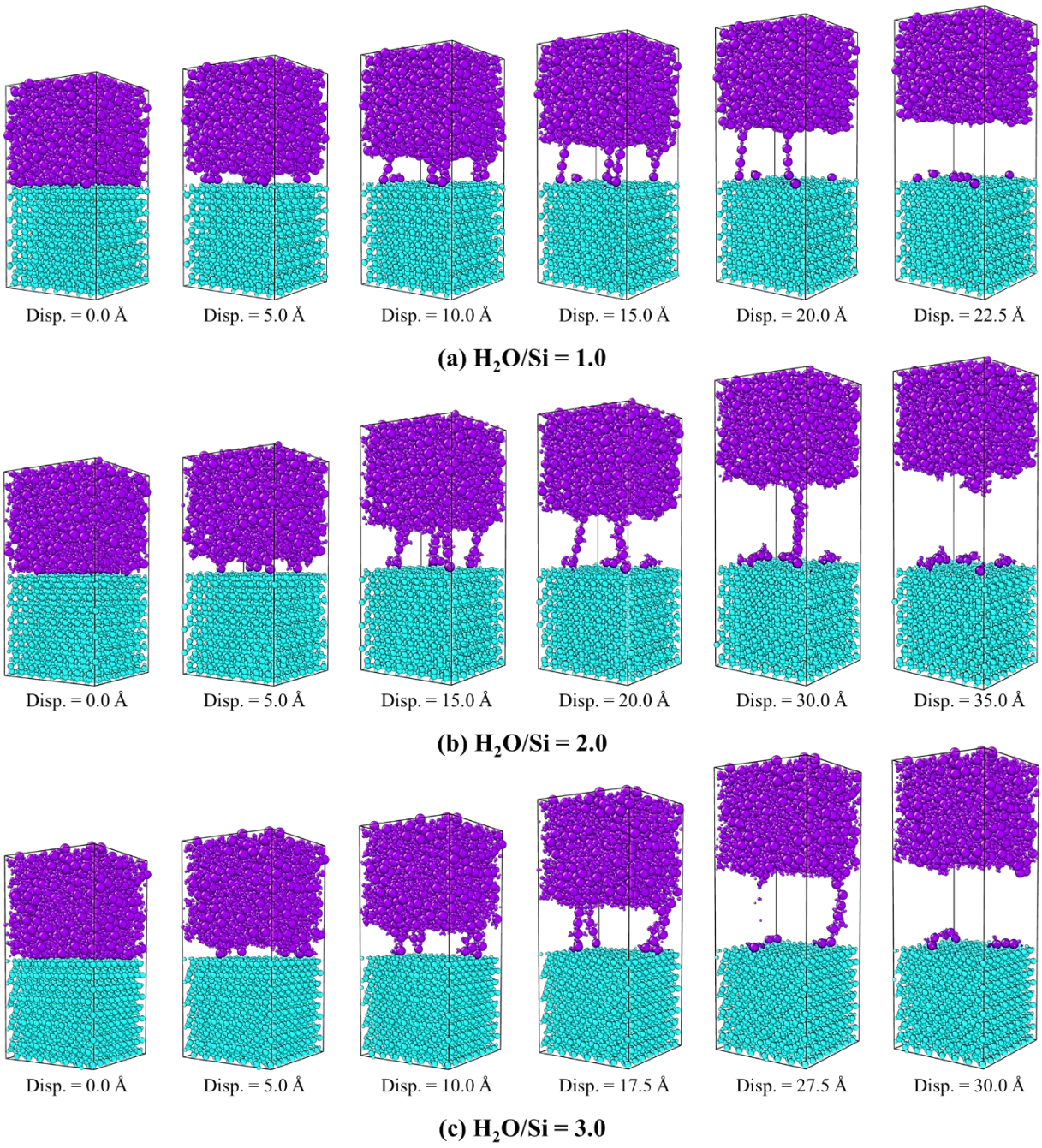

Fig. 7 Perspective views of the evolution of the C-S-H−silica systems during tensile loading for C-S-H with (a) H_2O/Si ratio = 1.0, (b) H_2O/Si ratio = 2.0, and (c) H_2O/Si ratio = 3.0. Note that only the deformed portion of the model systems is shown (the C-S-H atoms are in purple and the silica atoms are in blue).

The contribution of the atomic chains to the residual bond strength between C-S-H and silica was further studied by calculating the per-atom stress (σ_i) of the C-S-H−silica systems using the following equation:

$$\sigma_i = -m_i\vec{v}_i \otimes \vec{v}_i + \frac{1}{2}\sum_{j\neq i}^{N}(\vec{r}_{ij} \otimes \vec{F}_{ij}) \quad (3)$$

where m_i and $\vec{v}_i$ represent the mass and velocity vectors of the ith atom; $\vec{r}_{ij} = \vec{r}_{ij} - \vec{r}_{ij}$ is the relative position of atom i in relation to atom j, and $\vec{F}_{ij}$ is the force acting upon atom i due to interaction with atom j. Fig. 8 depicts the per-atom stress mapping of the local interfacial structure between C-S-H (H_2O/Si ratio of 1.0, 2.0 and 3.0) and silica during tensile loading. In Fig. 8 (a), it can be observed that two atomic chains were in tension. When one of the chains ruptured, the tensile stress was released from the chain (the atoms turned green), leaving the other chain to sustain more tensile stress (partial atoms turned red). When this chain ruptured, the tensile stress was also released. Similarly, in Fig 9 (b) and (c), the atomic chains also sustained the tensile stress during the tensile process, and the tensile stress was released when the chains ruptured. In addition, the atomic chains were composed of Ca^{2+}, OH^-, H_2O and silicates, all of which could be responsible for bearing the tensile stress, as labeled in Fig. 8. Therefore, the atomic chains transferred the stress between C-S-H and silica, and thus contributed to the residual strength of the interfacial structures at the fracture stage.

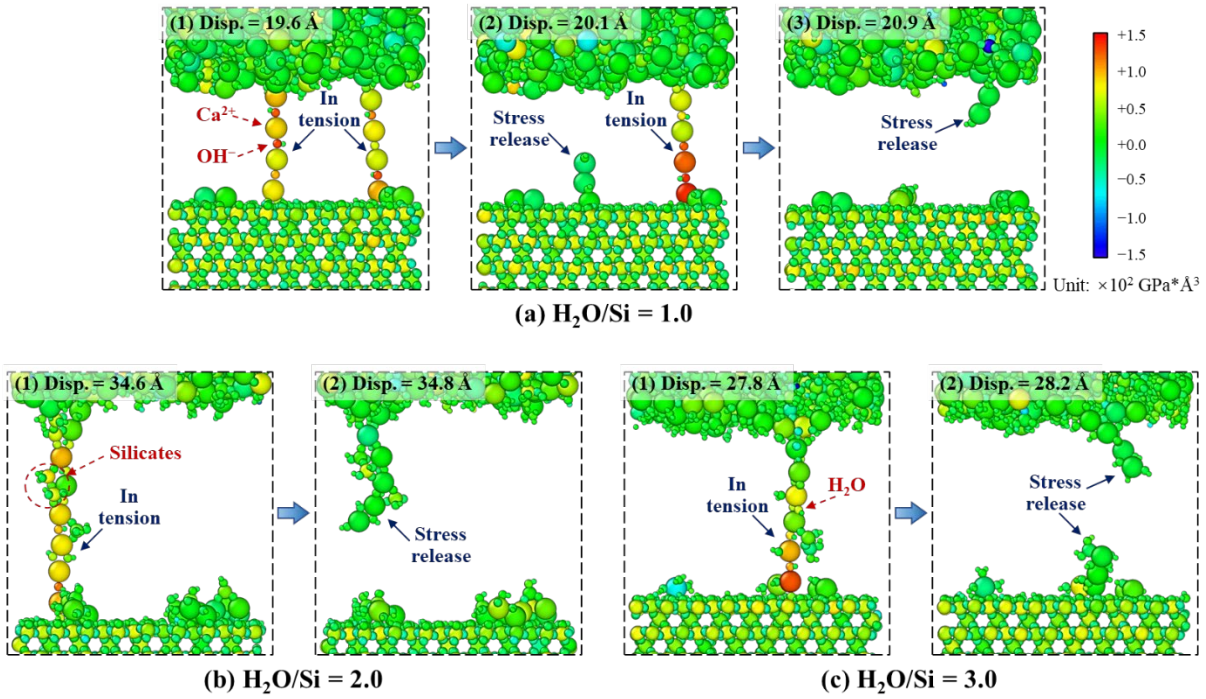

Fig. 8 Per-atom stress mapping on the local structures between C-S-H and silica during tensile loading: (a) H_2O/Si

ratio = 1.0 for C-S-H; (b) H_2O/Si ratio = 2.0 for C-S-H; (c) H_2O/Si ratio = 3.0 for C-S-H.

In addition, to illustrate the effect of the length scale of C-S-H−silica system on the fracture process, a larger interfacial structure (H_2O/Si ratio = 1.0) was established with twice the length in the x- and z-direction. Fig. 9(a) shows the snapshots of the fracture process of the larger C-S-H−silica system during the tensile process using the tensile method described in Fig. 6(a). Similarly, the fracture process of this larger interfacial structure also underwent three stages: crack propagation, atomic chain bridging through the C-S-H atoms, and complete failure (breakage of all atomic chains). Compared to the smaller case (Fig. 7a), it can be found that there exist more atomic chains that bridge the C-S-H and silica of the larger interfacial model, and the atomic chain bridging can last for a longer distance during the tensile process. Fig. 9(b) shows the pull force−displacement curve of this C-S-H−silica model. Compared to the smaller case, it is no doubt that the larger interfacial model had a higher peak load (162.1 nN), about 4 times higher than that (39.6 nN) of the smaller case. It proved that the interfacial strength was almost the same for the two cases. Due to the longer atomic chain bridging, it can be seen that the interfacial residual strength of the larger model can sustain for a longer distance.

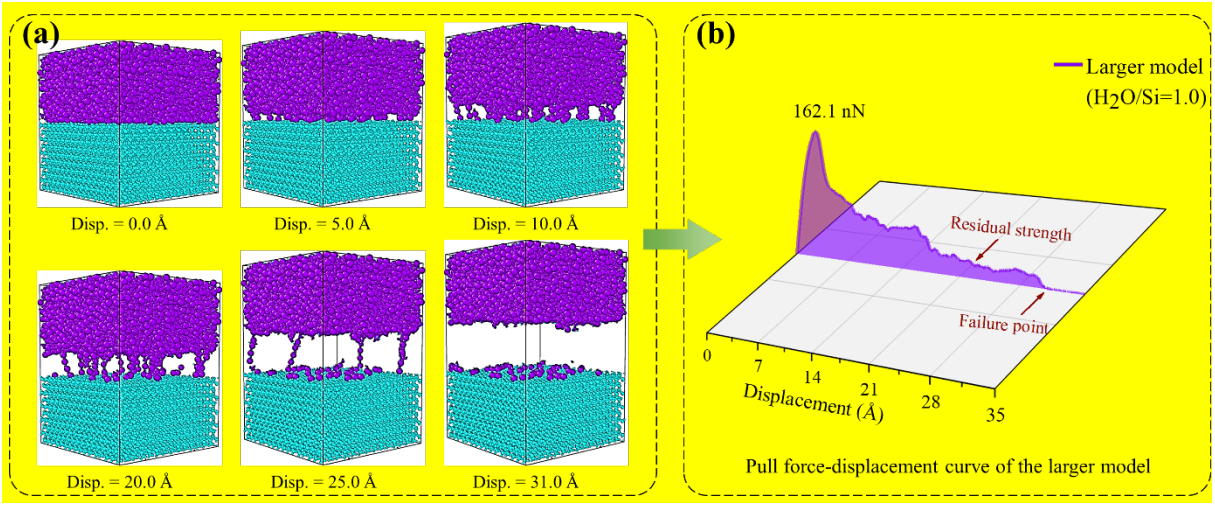

Fig. 9 (a) Perspective views of the fracture evolution of the larger C-S-H−silica model (H_2O/Si ratio = 1.0) during tensile loading; (2) Pull force−displacement curve of the larger C-S-H−silica model. The failure point occurred at 30.8 Å displacement.

4. Conclusions

The interfacial characteristics between cement paste and silica are far from being fully understood, especially from the nanoscale perspective. In this work, molecular models for the C-S-H−silica systems were developed, considering the influence of the water content of C-S-H. The following conclusions can be drawn from the atomistic simulations:

(1) Chemically, there were various types of bond schemes at the C-S-H−silica interface, including H-bonds and Ca−O ionic bonds. Increasing the water content of C-S-H increased the interfacial H-bond number, but decreased the interfacial Ca−O bond number. Moreover, there existed H^+ exchange between C-S-H and silica, and an increase in the water content of C-S-H could depress the deprotonation of the Si-OH groups on the silica surface.

(2) Structurally, an atomic-level ITZ with a low density was identified at the C-S-H–silica interface, which was attributed to the rich presence of –OH groups at the interface. By increasing the water content of C-S-H, the ITZ width increased slightly while the ITZ density decreased.

(3) Dynamically, the H_2O molecules and Ca^{2+} ions diffused in a faster rate in the ITZ than those in the bulk C-S-H. Increasing the water content of C-S-H accelerated the diffusion of the H_2O molecules and Ca^{2+} ions in the ITZ.

(4) Mechanically, the interfacial bond strength and residual strength between C-S-H and silica were inversely related to the water content of C-S-H because the interfacial interaction was weakened by increasing the water content of C-S-H. More specifically, the interfacial Coulomb potential (the main contributor of the interfacial interaction) was reduced by increasing the water content of C-S-H.

(5) Overall, the fracture process of the C-S-H–silica systems occurred in three stages: crack propagation, atomic chain bridging, and complete failure. The atomic chains between C-S-H and silica were composed of Ca^{2+}, OH^-, H_2O, and silicates, all of which could sustain the tensile stress and contributed to the residual bond strength of the structures at the fracture stage.

Declaration of competing interest

The authors declare that they have no known competing financial interests or personal relationships that could have appeared to influence the work reported in this paper.

Acknowledgments

The authors acknowledge the financial support received from the Hong Kong Research Grants Council—Theme-based Research Scheme with Grant No. T22-502/18-R, Guangdong Province R&D Plan for Key Areas with Grant No. 2019B111107002 and the NSFC/RGC Joint Research Scheme with Grant No. N_PolyU542/20, Start-up Fund for RAPs under the Strategic Hiring Scheme with Grant No. P0038964.

References

[1] T. Watari, Z. Cao, S. Hata, K. Nansai, Efficient use of cement and concrete to reduce reliance on supply-side technologies for net-zero emissions, Nature communications 13 (2022) 1-9.

[2] Y. Izumi, A. Iizuka, H.-J. Ho, Calculation of greenhouse gas emissions for a carbon recycling system using mineral carbon capture and utilization technology in the cement industry, Journal of Cleaner Production 312 (2021) 127618.

[3] B. Bose, C.R. Davis, K.A. Erk, Microstructural refinement of cement paste internally cured by polyacrylamide composite hydrogel particles containing silica fume and nanosilica, Cement and Concrete Research 143 (2021) 106400.

[4] B. Ali, L.A. Qureshi, S.U. Khan, Flexural behavior of glass fiber-reinforced recycled aggregate concrete and its impact on the cost and carbon footprint of concrete pavement, Construction and Building Materials 262 (2020) 120820.

[5] C. Signorini, A. Sola, B. Malchiodi, A. Nobili, A. Gatto, Failure mechanism of silica coated polypropylene fibres for Fibre Reinforced Concrete (FRC), Construction and Building Materials 236 (2020) 117549.

[6] H. Li, D. Zhao, M. Liebscher, B. Yin, J. Yang, M. Kaliske, V. Mechtcherine, An experimental and numerical study on the age depended bond-slip behavior between nano-silica modified carbon fibers and cementitious matrices, Cement and Concrete Composites 128 (2022) 104416.

[7] L. Hong, Y. Chen, T. Li, P. Gao, L. Sun, Microstructure and bonding behavior of fiber-mortar interface in fiber-reinforced concrete, Construction and Building Materials 232 (2020) 117235.

[8] M. Berra, F. Carassiti, T. Mangialardi, A. Paolini, M. Sebastiani, Effects of nanosilica addition on workability and compressive strength of Portland cement pastes, Construction and Building Materials 35 (2012) 666-675.

[9] C.M. Kansal, R. Goyal, Effect of nano silica, silica fume and steel slag on concrete properties, Materials Today: Proceedings 45 (2021) 4535-4540.

[10] H. Yang, M. Monasterio, D. Zheng, H. Cui, W. Tang, X. Bao, X. Chen, Effects of nano silica on the properties

of cement-based materials: a comprehensive review, Construction and Building Materials 282 (2021) 122715.

[11] Y. Gao, C. Hu, Y. Zhang, Z. Li, J. Pan, Investigation on microstructure and microstructural elastic properties of mortar incorporating fly ash, Cement and Concrete Composites 86 (2018) 315-321.

[12] K.L. Scrivener, A.K. Crumbie, P. Laugesen, The interfacial transition zone (ITZ) between cement paste and aggregate in concrete, Interface science 12 (2004) 411-421.

[13] K. Lyu, E. Garboczi, W. She, C. Miao, The effect of rough vs. smooth aggregate surfaces on the characteristics of the interfacial transition zone, Cement and Concrete Composites 99 (2019) 49-61.

[14] A.W. Pope, H.M. Jennings, The influence of mixing on the microstructure of the cement paste/aggregate interfacial zone and on the strength of mortar, Journal of materials science 27 (1992) 6452-6462.

[15] S. Erdem, A.R. Dawson, N.H. Thom, Impact load-induced micro-structural damage and micro-structure associated mechanical response of concrete made with different surface roughness and porosity aggregates, Cement and concrete research 42 (2012) 291-305.

[16] L. Zhang, Y. Zhang, C. Liu, L. Liu, K. Tang, Study on microstructure and bond strength of interfacial transition zone between cement paste and high-performance lightweight aggregates prepared from ferrochromium slag, Construction and Building Materials 142 (2017) 31-41.

[17] M. Nili, A. Ehsani, Investigating the effect of the cement paste and transition zone on strength development of concrete containing nanosilica and silica fume, Materials & Design 75 (2015) 174-183.

[18] A.N. Jam, N.N. Jam, M. Izadifar, T. Rabczuk, Molecular dynamics study on the crack propagation in carbon doped polycrystalline boron-nitride nanosheets, Computational Materials Science 203 (2022) 111066.

[19] R. Abadi, A. Jenabidehkordi, T. Rabczuk, Investigation into the fracture mechanism and thermal conductivity of borophene nanofilm; a reactive molecular dynamics simulation, Computational Materials Science 178 (2020) 109625.

[20] B. Mortazavi, M. Silani, E.V. Podryabinkin, T. Rabczuk, X. Zhuang, A.V. Shapeev, First‐Principles Multiscale Modeling of Mechanical Properties in Graphene/Borophene Heterostructures Empowered by Machine‐Learning Interatomic Potentials, Advanced Materials 33 (2021) 2102807.

[21] B. Javvaji, X. Zhuang, T. Rabczuk, B. Mortazavi, Machine‐Learning‐Based Exploration of Bending Flexoelectricity in Novel 2D Van der Waals Bilayers, Advanced Energy Materials 12 (2022) 2201370.

[22] R.J.-M. Pellenq, A. Kushima, R. Shahsavari, K.J. Van Vliet, M.J. Buehler, S. Yip, F.-J. Ulm, A realistic molecular model of cement hydrates, Proceedings of the National Academy of Sciences 106 (2009) 16102-16107.

[23] K. Liu, X. Cheng, Y. Ma, X. Gao, C. Zhang, Z. Li, J. Zhuang, Analysis of interfacial nanostructure and interaction mechanisms between cellulose fibres and calcium silicate hydrates using experimental and molecular dynamics simulation data, Applied Surface Science 506 (2020) 144914.

[24] J. Yang, D. Hou, Q. Ding, Ionic hydration structure, dynamics and adsorption mechanism of sulfate and sodium ions in the surface of calcium silicate hydrate gel: A molecular dynamics study, Applied Surface Science 448 (2018) 559-570.

[25] H. Manzano, A.K. Mohamed, R.K. Mishra, P. Bowen, A discussion on the paper “Role of porosity on the stiffness and stability of (001) surface of the nanogranular C–S–H gel”, Cement and Concrete Research 102 (2017) 227-230.

[26] H. Manzano, E. Masoero, I. Lopez-Arbeloa, H.M. Jennings, Shear deformations in calcium silicate hydrates, Soft Matter 9 (2013) 7333-7341.

[27] E. Duque-Redondo, K. Yamada, H. Manzano, Cs retention and diffusion in CSH at different Ca/Si ratio,

Cement and Concrete Research 140 (2021) 106294.
[28] N.A. Krishnan, B. Wang, G. Falzone, Y. Le Pape, N. Neithalath, L. Pilon, M. Bauchy, G. Sant, Confined water in layered silicates: the origin of anomalous thermal expansion behavior in calcium-silicate-hydrates, ACS Applied Materials & Interfaces 8 (2016) 35621-35627.
[29] D. Hou, J. Yu, Z. Jin, A. Hanif, Molecular dynamics study on calcium silicate hydrate subjected to tension loading and water attack: structural evolution, dynamics degradation and reactivity mechanism, Physical Chemistry Chemical Physics 20 (2018) 11130-11144.
[30] C. Ebbert, G. Grundmeier, N. Buitkamp, A. Kröger, F. Messerschmidt, P. Thissen, Toward a microscopic understanding of the calcium–silicate–hydrates/water interface, Applied surface science 290 (2014) 207-214.
[31] Y. Zhang, Q. Zhou, J.W. Ju, M. Bauchy, New insights into the mechanism governing the elasticity of calcium silicate hydrate gels exposed to high temperature: A molecular dynamics study, Cement and Concrete Research 141 (2021) 106333.
[32] D. Hou, H. Ma, Z. Li, Morphology of calcium silicate hydrate (CSH) gel: a molecular dynamic study, Advances in Cement Research 27 (2015) 135-146.
[33] M. Bauchy, M.A. Qomi, F.-J. Ulm, R.-M. Pellenq, Order and disorder in calcium–silicate–hydrate, The Journal of chemical physics 140 (2014) 214503.
[34] T. Du, H. Li, M. Bauchy, Molecular Dynamics Simulation of the Precipitation of Calcium Silicate Hydrate Nanostructures under Two-Dimensional Confinement by TiO2: Implications for Advanced Concretes, ACS Applied Nano Materials 3 (2020) 2176-2184.
[35] J. Fu, F. Bernard, S. Kamali-Bernard, Assessment of the elastic properties of amorphous calcium silicates hydrates (I) and (II) structures by molecular dynamics simulation, Molecular Simulation 44 (2018) 285-299.
[36] M.-F. Kai, J.-G. Dai, Understanding geopolymer binder-aggregate interfacial characteristics at molecular level, Cement and Concrete Research 149 (2021) 106582.
[37] D. Sun, J. Yan, X. Ma, M. Lan, Z. Wang, Z. Chen, S. Cui, Z. Wang, On the characterization of amine molecules behaviors in the nanochannels forming in calcium silicate hydrate gel, Applied Surface Science 560 (2021) 149994.
[38] M.R. Sadat, K. Muralidharan, L. Zhang, Reactive molecular dynamics simulation of the mechanical behavior of sodium aluminosilicate geopolymer and calcium silicate hydrate composites, Computational Materials Science 150 (2018) 500-509.
[39] J. Rimsza, J. Du, Interfacial structure and evolution of the water–silica gel system by reactive force-field-based molecular dynamics simulations, The Journal of Physical Chemistry C 121 (2017) 11534-11543.
[40] Y. Bai, H. Sui, X. Liu, L. He, X. Li, E. Thormann, Effects of the N, O, and S heteroatoms on the adsorption and desorption of asphaltenes on silica surface: A molecular dynamics simulation, Fuel 240 (2019) 252-261.
[41] M. Ebadi, L.T. Costa, C.M. Araujo, D. Brandell, Modelling the Polymer Electrolyte/Li-Metal Interface by Molecular Dynamics Simulations, Electrochimica Acta 234 (2017) 43-51.
[42] Y. Li, Q. Wang, S. Wang, A review on enhancement of mechanical and tribological properties of polymer composites reinforced by carbon nanotubes and graphene sheet: molecular dynamics simulations, Composites Part B: Engineering 160 (2019) 348-361.
[43] H. Talebi, M. Silani, S. Bordas, P. Kerfriden, T. Rabczuk, A computational library for multiscale modeling of material failure, Computational Mechanics 53 (2014) 1047-1071.
[44] B. Mortazavi, H. Yang, F. Mohebbi, G. Cuniberti, T. Rabczuk, Graphene or h-BN paraffin composite structures for the thermal management of Li-ion batteries: A multiscale investigation, Applied energy 202

(2017) 323-334.

[45] Y. Zhou, Z.-c. Peng, J.-l. Huang, T. Ma, X.-m. Huang, C.-w. Miao, A molecular dynamics study of calcium silicate hydrates-aggregate interfacial interactions and influence of moisture, Journal of Central South University 28 (2021) 16-28.

[46] L. Zhuravlev, The surface chemistry of amorphous silica. Zhuravlev model, Colloids and Surfaces A: Physicochemical and Engineering Aspects 173 (2000) 1-38.

[47] L. Zhuravlev, Concentration of hydroxyl groups on the surface of amorphous silicas, Langmuir 3 (1987) 316-318.

[48] G. Xu, H. Wang, Molecular dynamics study of interfacial mechanical behavior between asphalt binder and mineral aggregate, Construction and Building Materials 121 (2016) 246-254.

[49] Z. Dong, Z. Liu, P. Wang, X. Gong, Nanostructure characterization of asphalt-aggregate interface through molecular dynamics simulation and atomic force microscopy, Fuel 189 (2017) 155-163.

[50] W. Sun, H. Wang, Moisture effect on nanostructure and adhesion energy of asphalt on aggregate surface: A molecular dynamics study, Applied Surface Science 510 (2020) 145435.

[51] L. Chu, L. Luo, T. Fwa, Effects of aggregate mineral surface anisotropy on asphalt-aggregate interfacial bonding using molecular dynamics (MD) simulation, Construction and Building Materials 225 (2019) 1-12.

[52] S.V. Patwardhan, F.S. Emami, R.J. Berry, S.E. Jones, R.R. Naik, O. Deschaume, H. Heinz, C.C. Perry, Chemistry of aqueous silica nanoparticle surfaces and the mechanism of selective peptide adsorption, Journal of the American Chemical Society 134 (2012) 6244-6256.

[53] X. Cong, R.J. Kirkpatrick, 29Si MAS NMR study of the structure of calcium silicate hydrate, Advanced Cement Based Materials 3 (1996) 144-156.

[54] E. Duque-Redondo, P.A. Bonnaud, H. Manzano, A comprehensive review of CSH empirical and computational models, their applications, and practical aspects, Cement and Concrete Research 156 (2022) 106784.

[55] M. Abdolhosseini Qomi, K. Krakowiak, M. Bauchy, K. Stewart, R. Shahsavari, D. Jagannathan, D.B. Brommer, A. Baronnet, M.J. Buehler, S. Yip, Combinatorial molecular optimization of cement hydrates, Nature communications 5 (2014) 1-10.

[56] A. Zhou, Z. Yu, H. Wei, L.-h. Tam, T. Liu, D. Zou, Understanding the toughening mechanism of silane coupling agents in the interfacial bonding in steel fiber-reinforced cementitious composites, ACS Applied Materials & Interfaces 12 (2020) 44163-44171.

[57] H.J. Berendsen, J.v. Postma, W.F. Van Gunsteren, A. DiNola, J.R. Haak, Molecular dynamics with coupling to an external bath, The Journal of chemical physics 81 (1984) 3684-3690.

[58] M.A. Qomi, K. Krakowiak, M. Bauchy, K. Stewart, R. Shahsavari, D. Jagannathan, D.B. Brommer, A. Baronnet, M.J. Buehler, S. Yip, Combinatorial molecular optimization of cement hydrates, Nature communications 5 (2014) 1-10.

[59] M.F. Kai, L.W. Zhang, K.M. Liew, New insights into creep characteristics of calcium silicate hydrates at molecular level, Cement and Concrete Research 142 (2021) 106366.

[60] M.F. Kai, L.W. Zhang, K.M. Liew, Graphene and graphene oxide in calcium silicate hydrates: Chemical reactions, mechanical behavior and interfacial sliding, Carbon 146 (2019) 181-193.

[61] A.C. Van Duin, S. Dasgupta, F. Lorant, W.A. Goddard, ReaxFF: a reactive force field for hydrocarbons, The Journal of Physical Chemistry A 105 (2001) 9396-9409.

[62] K. Chenoweth, A.C. Van Duin, W.A. Goddard, ReaxFF reactive force field for molecular dynamics simulations of hydrocarbon oxidation, The Journal of Physical Chemistry A 112 (2008) 1040-1053.

[63] K.L. Joshi, G. Psofogiannakis, A.C. Van Duin, S. Raman, Reactive molecular simulations of protonation of water clusters and depletion of acidity in H-ZSM-5 zeolite, Physical Chemistry Chemical Physics 16 (2014) 18433-18441.

[64] H. Manzano, R.J. Pellenq, F.-J. Ulm, M.J. Buehler, A.C. Van Duin, Hydration of calcium oxide surface predicted by reactive force field molecular dynamics, Langmuir 28 (2012) 4187-4197.

[65] A.C. Van Duin, A. Strachan, S. Stewman, Q. Zhang, X. Xu, W.A. Goddard, ReaxFFSiO reactive force field for silicon and silicon oxide systems, The Journal of Physical Chemistry A 107 (2003) 3803-3811.

[66] R. Shahsavari, R.J.-M. Pellenq, F.-J. Ulm, Empirical force fields for complex hydrated calcio-silicate layered materials, Physical Chemistry Chemical Physics 13 (2011) 1002-1011.

[67] W. Orellana, A.J. da Silva, A. Fazzio, O 2 Diffusion in SiO 2: Triplet versus Singlet, Physical review letters 87 (2001) 155901.

[68] D. Hou, Z. Ding, P. Wang, M. Wang, Q. Xu, X. Wang, J. Guan, Y. Su, Y. Zhang, Influence of Cu Doping on the Hydration of Dicalcium Silicate: A First-Principles Study, ACS Sustainable Chemistry & Engineering (2022).

[69] B.M. Lowe, C.-K. Skylaris, N.G. Green, Acid-base dissociation mechanisms and energetics at the silica–water interface: An activationless process, Journal of colloid and interface science 451 (2015) 231-244.

[70] B. Li, N. Li, H. Brouwers, Q. Yu, W. Chen, Understanding hydrogen bonding in calcium silicate hydrate combining solid-state NMR and first principle calculations, Construction and Building Materials 233 (2020) 117347.

[71] M.S. Azam, C.N. Weeraman, J.M. Gibbs-Davis, Specific cation effects on the bimodal acid–base behavior of the silica/water interface, The journal of physical chemistry letters 3 (2012) 1269-1274.

[72] Z. Wang, Q. Lv, S. Chen, C. Li, S. Sun, S. Hu, Effect of interfacial bonding on interphase properties in SiO2/epoxy nanocomposite: a molecular dynamics simulation study, ACS applied materials & interfaces 8 (2016) 7499-7508.

[73] W.M. Ji, L.W. Zhang, K.M. Liew, Understanding interfacial interaction characteristics of carbon nitride reinforced epoxy composites from atomistic insights, Carbon 171 (2021) 45-54.